Synthetic Phase Variation for Engineered Microbial Consortia

Matthieu F. Kratz[1], Richard M. Murray[1] and Michael B. Elowitz[1*]

Division of Biology and Biological Engineering, California Institute of Technology, Pasadena, CA
*To whom correspondence should be addressed: melowitz@caltech.edu

Abstract

Some biochemical functions can be performed more efficiently when split into different tasks, each performed by distinct strains within a microbial consortium. Due to the distinct growth dynamics of each strain, uncontrolled consortia have unstable composition dynamics, leading to the rapid loss of the community level function. Several approaches have been developed to stabilize consortia, with most relying on communicated-mediated growth and death feedback. These approaches require accurate communication between strains to maintain control, something which is not guaranteed under non-well-mixed conditions. As such, these methods are of limited utility in consortia applications with poorly mixed environments e.g. industrial scale bioreactors or soil. Here, inspired by microbial phase variation dynamics, we introduce an alternative, communication-free approach in which a set of genetically identical cells switch stochastically between distinct phenotypes. In this scheme, the population composition is dynamically stable and determined by the rates of transitions between states. Mathematical modeling indicates that this approach can stabilize consortia. Experimentally, we used reversible DNA inversions catalyzed by serine recombinases to implement a dynamic consortium. We then characterized the dynamic properties of the consortium at the single cell and bulk levels, and demonstrated control in 2- and 3-state consortia. These results provide a composition control approach that does not rely on cell to cell communication, providing a foundation for deployment of engineered consortia in complex, and sometimes non-mixed, environments such as industrial scale bioreactors or the human gut.

Introduction

Consortia are communities composed of multiple distinct cell types[1–3] that coordinate their individual behavior to achieve a community-level function. Consortia could implement more complex functions than single strain systems, and enable applications in metabolic engineering and biomanufacturing[4–8]. To this end, a major research goal in microbial synthetic biology has been to extend synthetic gene networks to the consortia level. The standard way to create a consortium is to co-culture several distinct microbial strains implementing separate parts of an overall function[1–3,7], such as metabolic synthesis of a chemical (Fig. 1a, left). In such systems, optimizing the overall consortium function requires a mechanism to optimize and maintain stable strain composition[1,5,9]. One approach is to use naturally symbiotic strains. However, many applications favor highly engineered and specialized lab strains[10,11]. As a result, even small differences in the growth rates of the individual strains can drastically shift the composition[2,3,7] (Fig. 1b, left).

Several approaches have been introduced to control consortium composition. One approach is to establish feedback on population sizes through intercellular signaling systems (Fig. 1a, center, Fig. 1b right)[12–18]. Broadly speaking, each consortium member secretes a member-specific signal that influences the growth or death rates of other members. For instance, auxotrophic *E. coli* mutants were used to create pairs of strains that complement each other's growth through cross-feeding of essential metabolites[18]. Metabolites secreted from one auxotrophic strain directly stimulate the growth of a complementary auxotrophic strain, favoring co-existence. In this case, the metabolites act as signals and controllers of growth rates. Recent implementations have expanded the repertoire of metabolites used this way[15] and exploited quorum sensing molecules and toxin-antitoxin systems for communication and death control[12,13,16], respectively. These approaches allow for inter-species consortia but require accurate communication between members to properly function[1,4]. As such, their performance can be compromised in non-well-mixed settings e.g. industrial bioreactors[19] or human gut[20]. Furthermore, they rely on a limited set of orthogonal communication channels, making scaling to many members difficult. Hence, these communication-mediated approaches have substantial limitations in terms of their scalability and suitability for non-well-mixed deployment contexts.

Another recent class of approaches addresses this scaling issue by emulating stem cell differentiation dynamics and removing the need for intercellular communication[21–23]. In these approaches, a consortium starts as a set of undifferentiated progenitor cells and progressively shifts to a community of terminally differentiated cells. Recently, *An et al.* used several orthogonal serine recombinases to mediate differentiation into a series of terminal cell types from a single founder cell type[23]. By manipulating the nucleotide sequence of recombinase attachment sites, the precise ratio of the terminal cell types could be manipulated. This approach is scalable to many phenotypes, but is limited by depletion of the progenitor pool and lacks closed-loop feedback control of overall cell fate proportions.

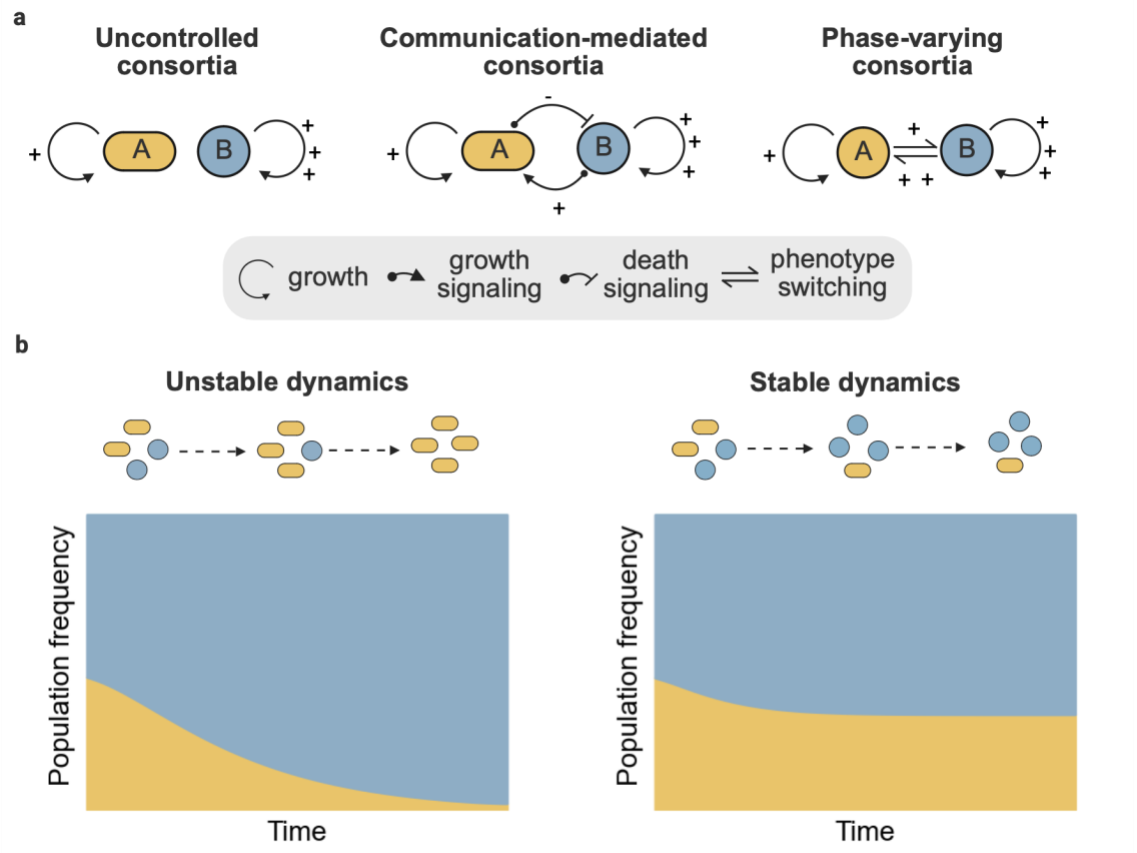

Figure 1. Mechanisms and dynamics of microbial consortia implementations.
a Schematics of different microbial consortia implementations: (left) no composition control, (middle) communication-based composition control, where growth and death are mediated via cell to cell signalling, and (right) phase-varying consortia, where each cell stochastically switches between phenotypic states. **b** Bulk population dynamics of consortia implementations. In an uncontrolled system, the fastest growing strain dominates the culture (unstable dynamics). Both the communication-mediated and phase-varying consortia balance all strains, achieving stable dynamics. Blue and yellow represent distinct states, while shapes (circle, oval) represent distinct strains.

What approaches could allow for scalable and continual composition control without relying on intercellular communication? In the natural process of phase variation, cells stochastically and reversibly transition between distinct phenotypic states[24,25], each conferring distinct fitness benefits and costs. Phase variation facilitates survival in environments with abrupt and stochastic changes in selection pressure[24–26]. Here, we implement a synthetic version of phase variation in which a single strain encodes a set of mutually exclusive states, with each individual cell stochastically and reversibly switching between these states (Fig. 1a, right, Fig. 1b right). By controlling state transition rates, the system allows tuning of the equilibrium distribution. In this approach, there is no requirement for intercellular communication and cells have access to all states at all times. These features make this system amenable to continuous control of composition.

We first used mathematical modeling to demonstrate that the dynamics of phase variation can stabilize otherwise unstable consortium configurations. We then designed circuits that exploit reversible recombinase flipping to switch between mutually exclusive phenotypic states. Next, we experimentally constructed this design, showing it can balance the abundances of two distinct states. Finally, through the addition of a secondary orthogonal recombinase, we demonstrated that synthetic phase variation can be scaled to control the proportions of three distinct states. This work establishes a communication-free, scalable architecture for continuous control of consortia composition, opening the door to applications of consortia in otherwise inaccessible contexts.

Results

Phase variation stabilizes otherwise unstable consortium *in silico*

Under what circumstances can stochastic switching establish a stable consortium? To address this question, we constructed a simple mathematical model representing the population sizes of cells in two states, denoted A, B in a well-mixed, chemostatic environment. Nutrients (S) are supplied, and cells and media are removed, at the dilution rate, D. Cells divide at rate μ. In general, cells compete for the limited nutrient supply.

Using this framework, we first examined the case of an uncontrolled consortium with two competing strains, each fixed in a distinct state, A or B. For example, if strain B grows at a 30% faster rate than strain A, and both strains are seeded at equal concentrations, the combination of growth rate differences and limiting nutrient leads strain B to progressively overtake the mixed culture (Fig. 2a). Thus, in the absence of additional control mechanisms, the consortium is unstable.

Phase variation mitigates this issue. To explore this, we added a secondary layer of phase variation dynamics to the model. In this case, the two phenotypic states, A and B, interconvert, with switching rates[27–29] β_1 or β_2 for B-to-A, or A-to-B transitions, respectively (Fig. 2b, modeling supplement). Transitions compensate for the growth advantage of B, allowing for stable coexistence of both states (Fig. 2b) with a population ratio, r (Equation 1), that depends on the switching rates, dilution, and growth rates:

$$r = \frac{A}{B} = \frac{\alpha + \sqrt{\alpha^2 + 4\mu_b \beta_1 \beta_2}}{2\beta_2}, \qquad (1)$$

$$\alpha = (1 - \mu_b)D + \beta_1 - \mu_b \beta_2 .$$

Thus, r takes on a unique population ratio that can be modulated by tuning switching rates (Supplementary Fig. 1). Overall, this model demonstrates how phase variation can force co-existence in an otherwise unstable consortia and allow to tune the relative abundance of consortia members.

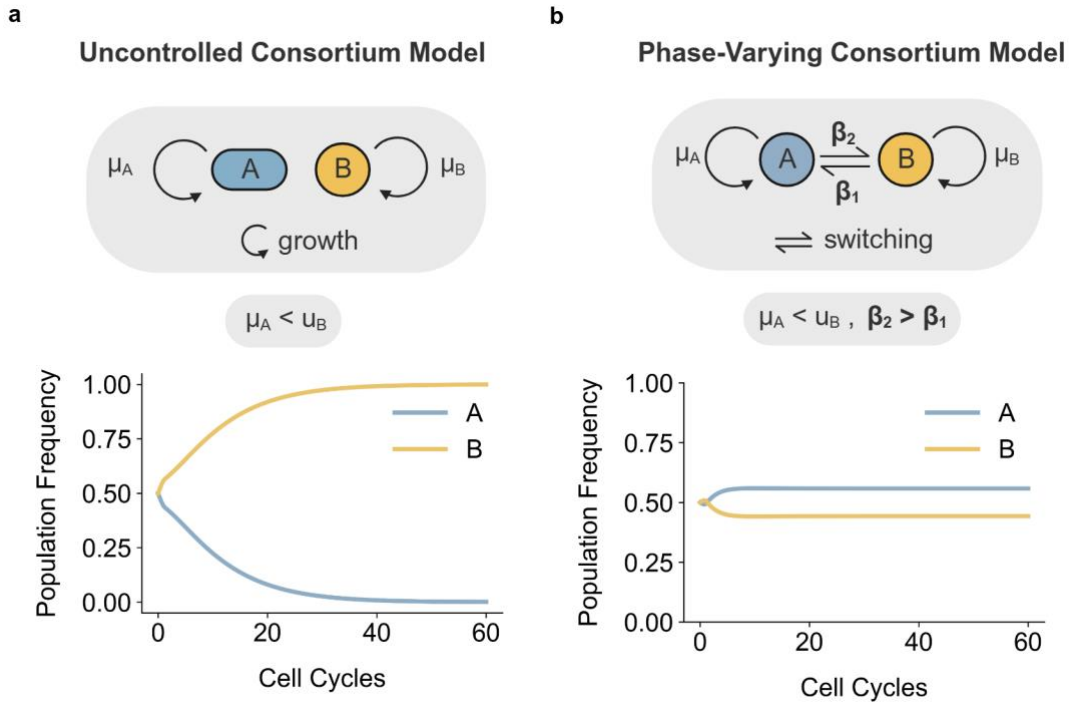

Figure 2. Phase variation stabilizes consortium composition. a Uncontrolled consortium model schematic and simulation results. **b** Phase-varying consortium model schematic and simulation results. Presented results and parameters are non-dimensionalized and scaled to the growth rate of strain/phenotype A. Further details of models, parameters and simulations can be found in the modeling supplement.

151 **A recombinase circuit can drive 2-state phase variation dynamics**
152
153 Having demonstrated that phase variation dynamics can stabilize consortia *in silico,* we sought to
154 design an experimental circuit that implements phase variation. The ideal circuit would rely on
155 well-characterized components with multiple orthogonal variants to enable scalable engineering
156 of systems with multiple states. We designed a DNA cassette which encodes two mutually
157 exclusive transcriptional states, one corresponding to YFP[30] expression and the other to
158 mTurquoise[31] expression (Fig. 3a). Both fluorophores were tagged with the ssrA degradation tag,
159 shortening their half-lives to accelerate circuit readout dynamics[32]. To allow transitions, we also
160 incorporated serine recombinases, viral proteins that catalyze site specific DNA
161 rearrangements[33]. We flanked the cassette with two antiparallel Bxb1 serine recombinase
162 attachment sites. When Bxb1 binds to these sites, it catalyzes inversion of the intervening DNA
163 sequence, switching expression from YFP to mTurquoise. This reaction can be reversed by Bxb1
164 in complex with its cognate reverse directionality factor (RDF)[34]. By regulating the concentrations
165 of Bxb1 and its RDF, one can influence the frequency and bias of these flipping reactions[35].
166 Analogous constructs have been previously used as rewritable DNA storage[36–38] or to tune
167 expression variation of a single gene[39].
168
169 After constructing this circuit, we experimentally probed its single cell dynamics using the 'mother
170 machine' microfluidic device[40–44] (Fig. 3b). This device consists of a series of growth channels
171 perpendicular to a trench through which fresh media flows, providing a chemostatic environment
172 and allowing long term monitoring of individual "mother" cells at the ends of each channel. This
173 device thus allows one to probe the long term switching dynamics of single cells under steady
174 state conditions.
175
176 When observed in the mother machine, individual cells stably expressed a single fluorophore for
177 multiple cell cycles, while occasionally switching to the other state. We can see an example of
178 this switching process in Fig. 3c, in which a cell switches from mTurquoise to YFP fluorescence
179 (Supplemental Movie 1). It is important to note that in this instance, the mother cell seems to
180 spend relatively little time in a mixed YFP-mTurquoise state, existing primarily in one of the two
181 states exclusively.
182
183 To further probe the switching dynamics, we tracked the distribution of residence times, defined
184 as how long the cell spends in a given state before switching (Fig. 3d). Both states displayed a
185 wide distribution of residence times. Because the switching rates were unequal, cells spent more
186 time in the YFP state (residence time of 521 min., s.d. 300 min) than the mTurquoise state (174
187 min., s.d. 119 min). Furthermore, consistent with the kymograph observations, the YFP and
188 mTurquoise states were exclusive, with cells spending relatively little time in transitional states
189 expressing both proteins. The residence times were exponentially distributed for both the
190 mTurquoise and YFP states, but with different time constants, consistent with our expectation of
191 a generative Poisson process for switching (Supplementary Fig. 2).

192

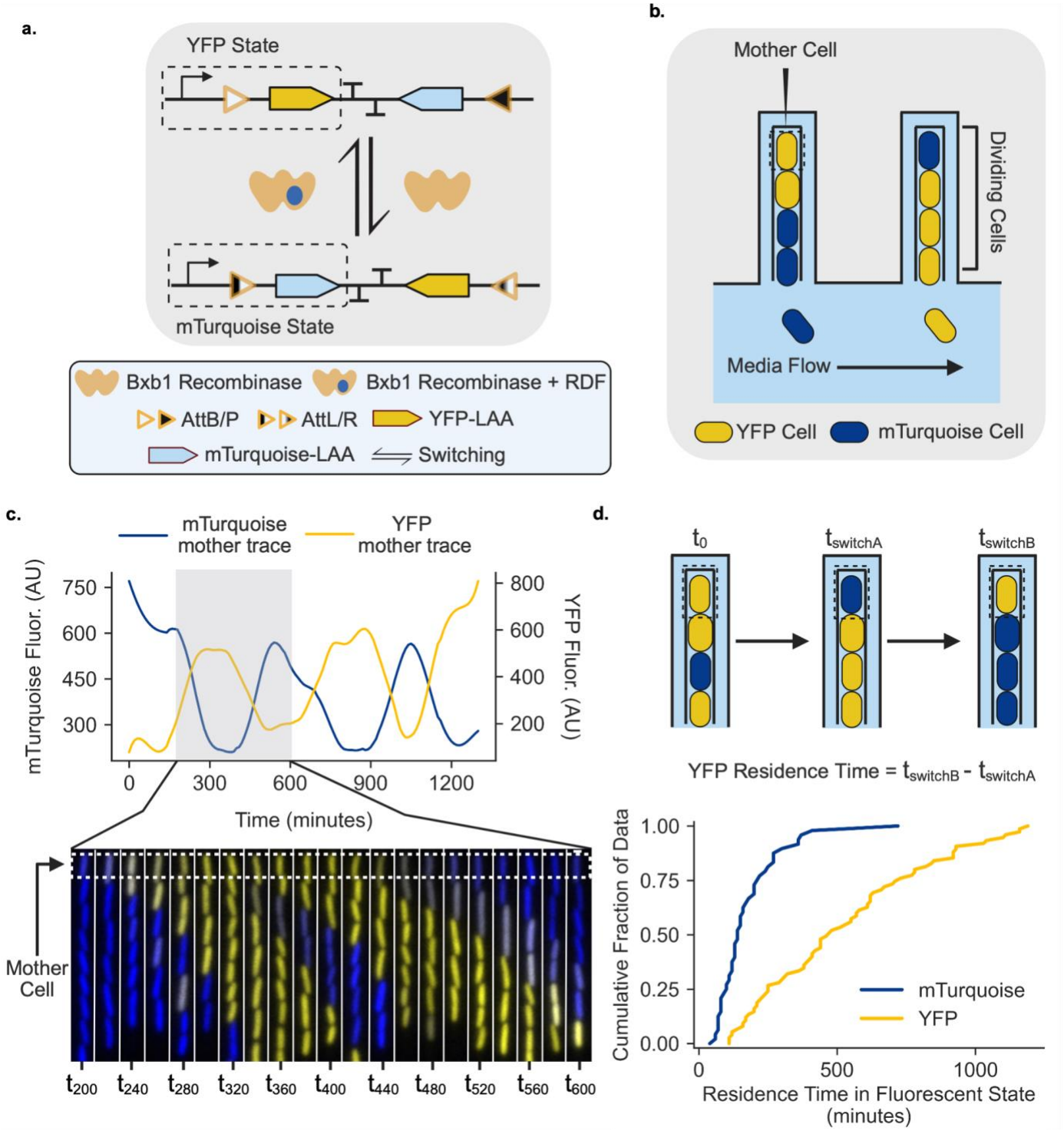

193

194 **Figure 3. A recombinase circuit successfully recreates single cell phase variation**
195 **dynamics. a** Recombinase switching construct schematic. The arrows represent state
196 transitions, with Bxb1 or the Bxb1-RDF complex catalyzing transitions. Bxb1 recombinase was

197 destabilized using the LAA ClpXP degradation tag[32]. This construct was integrated as a single
198 copy in the genome. Bxb1 and RDF were expressed under inducible control from a separate
199 plasmid. **b** Mother machine schematic. The cell at the end of the growth channel (mother cell),
200 remains in the channel indefinitely and can be tracked for many generations **c** Mother machine
201 kymograph and single mother cell fluorescence trace. Successive images in the kymograph are
202 separated by twenty minute intervals. The highlighted grey section in the trace corresponds to the
203 time frame associated with the kymograph movie. **d** Schematic defining residence times and
204 cumulative distribution of mother cell residence times. Data were collected by manual observation
205 of mother cells.
206

207 **Varying expression of recombinase elements enables bulk composition control**
208
209 We next sought to tune the state composition of the population. We placed Bxb1 and Bxb1 RDF
210 under the control of salicylate (sal) and Isopropyl-β-d-thiogalactoside (IPTG) inducible
211 promoters[45], respectively, on a p15a plasmid (Fig. 4a). With these constructs, the transition rates
212 that govern the bulk cell population dynamics should be tunable, allowing for bulk-scale control of
213 composition.
214
215 We used the mother machine to observe population dynamics under YFP-biased (0 μM sal, 250
216 μM IPTG) and Turquoise-biased (4 μM sal, 10 μM IPTG) inducer conditions. The circuit was
217 strongly biased to the mTurquoise state in the absence of inducers due to basal Bxb1 expression.
218 Upon induction, the distribution of cell states rapidly shifted to a new steady-state composition
219 (Fig. 4b, Supplementary Fig. 3-4). Within ~19 hours both conditions reached 95% of the steady-
220 state composition value. Additionally, we tracked the frequency of mixed-state cells during these
221 runs (Supplementary Fig. 5) and noted that at steady state, the frequency of these cells remained
222 ~5%, further supporting our previous findings that most cells exist in a single expression state.
223 Together, these results indicate that Bxb1 and RDF expression levels can tune the population
224 composition.
225
226 To rapidly explore a broader range of inducer concentrations, we switched to a turbidostat-plate
227 reader setup that allows greater multiplexing (Fig. 4c). The non-chemostatic plate reader
228 conditions also provided an opportunity to examine circuit operation in a distinct, batch culture
229 growth context.
230
231 For plate reader experiments, we explored a matrix of 3 initial compositions, each induced with
232 one of 5 different inducer concentrations, for a total of 15 individual culture trajectories (Fig. 4c,
233 Supplementary Fig. 7-11). For each inducer concentration, cultures approached the same final
234 steady state distribution regardless of initial conditions, and did so over a similar timescale (Fig.
235 4c). Final compositions spanned a ~100-fold range of population ratios, and were tunable within
236 this range. In a negative control experiment, we performed a similar analysis on a 2-strain (non-
237 switching) system. In this case, cultures were overtaken by the YFP expressing strain
238 (Supplementary Fig. 6), indicating that the circuit is required to stabilize mixed compositions.
239
240 The time to reach 95% of the steady state was noticeably longer in the plate reader (~19 h)
241 compared to the mother machine (~26 h). However, the final compositions were similar between
242 the two environments — 1.08 vs. 1.05 for the YFP-biased condition and -0.91 vs. -0.66 for the
243 mTurquoise-biased condition. Taken together, these results demonstrated continuous control of
244 bulk composition dynamics.
245

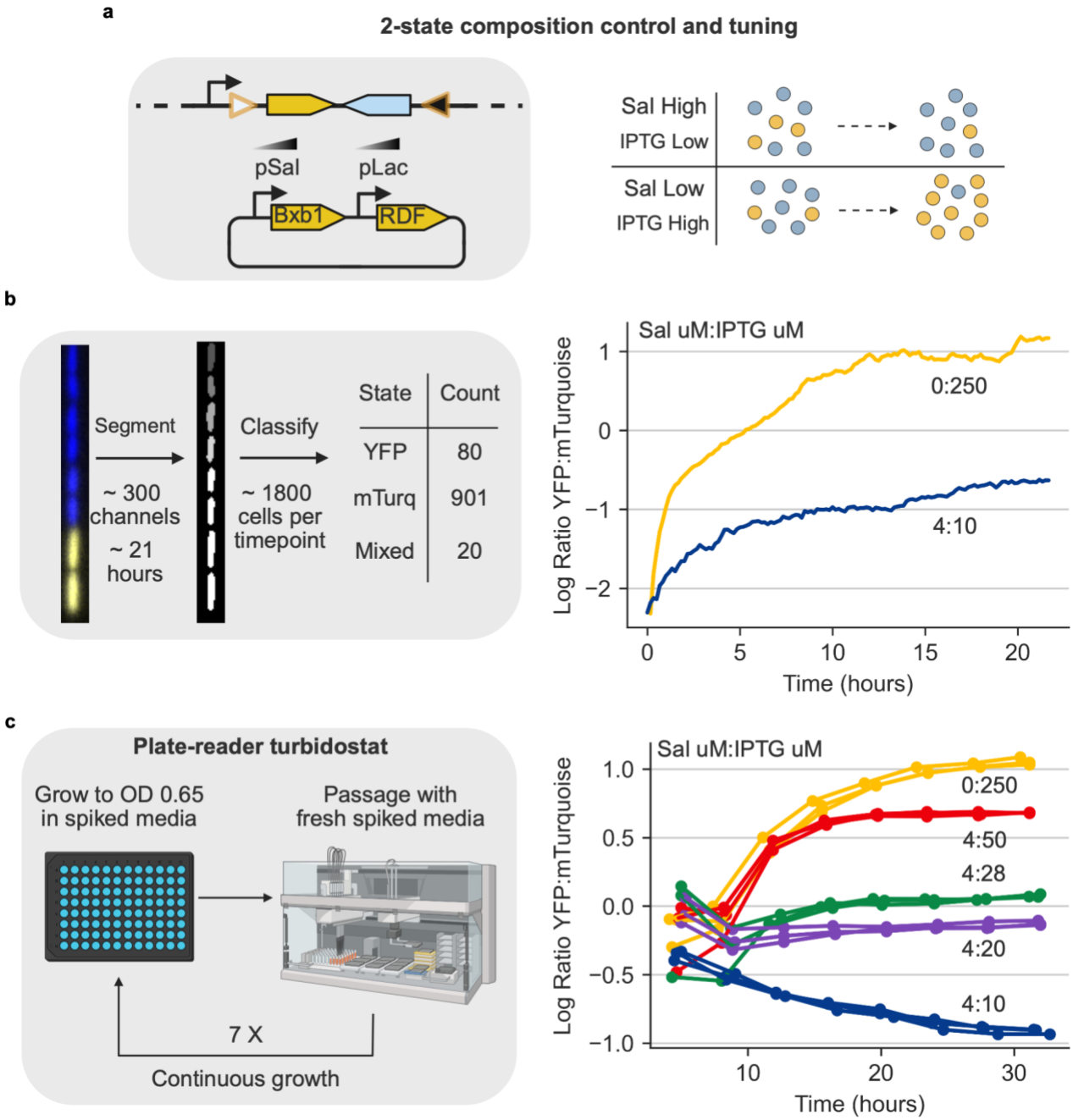

Figure 4. Synthetic phase variation enables bulk composition control in diverse growth contexts a 2-state composition control schematic. The recombinase switching construct was located in a single copy on the genome and the recombinase elements were expressed from a p15a plasmid. Bxb1 is controlled by a salicylate inducible promoter (pSal) and its cognate RDF is controlled by an IPTG inducible promoter pTac. By varying inducer levels, the steady state composition of the system should be tunable. **b** Mother machine processing pipeline and bulk population dynamics. Cells are sorted into YFP and mTurquoise categories based on the median

254 fluorescent signal ratio of the relevant channels. Traces start in a heavily mTurquoise biased state
255 due to leak associated with the Bxb1 recombinase. The inducer concentrations used for each
256 experiment are labeled next to each trace. Individual population traces can be found in
257 Supplementary Fig. 2-3. **c** Plate reader turbidostat setup and bulk population dynamics. Traces
258 of the same color are cultured in the same media and expected to end at the same final
259 composition. The inducer concentrations used for each experiment are labeled next to each trace.
260 Due to the dynamics of degradation-tagged fluorophores in batch cultures, the maximum value
261 for each fluorophore channel in each cycle was used to calculate composition. Signals are
262 normalized to the max fluorescence possible for a given channel e.g. YFP is normalized to an all
263 YFP culture.

264 **A second recombinase enables 3-state phase variation**
265
266 Many consortium applications primarily use two strains, but recent use cases in metabolic
267 engineering employed as many as four distinct strains[46]. This work provokes the question of
268 whether synthetic phase variation can scale to larger numbers of states[47,48]. In fact, incorporation
269 of a second orthogonal recombinase (blue) can enable 3-state switching. As shown in Fig. 5a, we
270 added a third transcriptional state downstream of the 2-state unit, and flanked the construct with
271 the attachment sites of the second recombinase. The resulting system is predicted to generate
272 four genetic states, one for state A, one for state B and two for state C (C_A and C_B). These two C
273 states both express the C gene and are therefore phenotypically equivalent. However, they
274 respond differently to the second (blue) recombinase, with C_A and C_B respectively transitioning to
275 states A and B. In this design, the first recombinase activity (yellow) determines the ratio of A to
276 B population sizes, while the second recombinase (blue) determines the (A+B) to C ratio. We
277 refer to the system as the 3-state circuit based on the number of distinct phenotypic states.
278
279 To understand composition control properties of the 3-state circuit, we simulated its dynamics
280 using the framework in Fig. 2 (Fig. 5b, modeling supplement). State-switching in the 3-state
281 architecture stabilizes configurations that would otherwise be unstable (Fig. 5c). Depending on
282 switching rates, the circuit can access the full repertoire of possible cell state compositions
283 (Supplementary Fig. 12). Overall, these mathematical modeling results imply that our design can
284 be scaled beyond the control of 2-states.
285

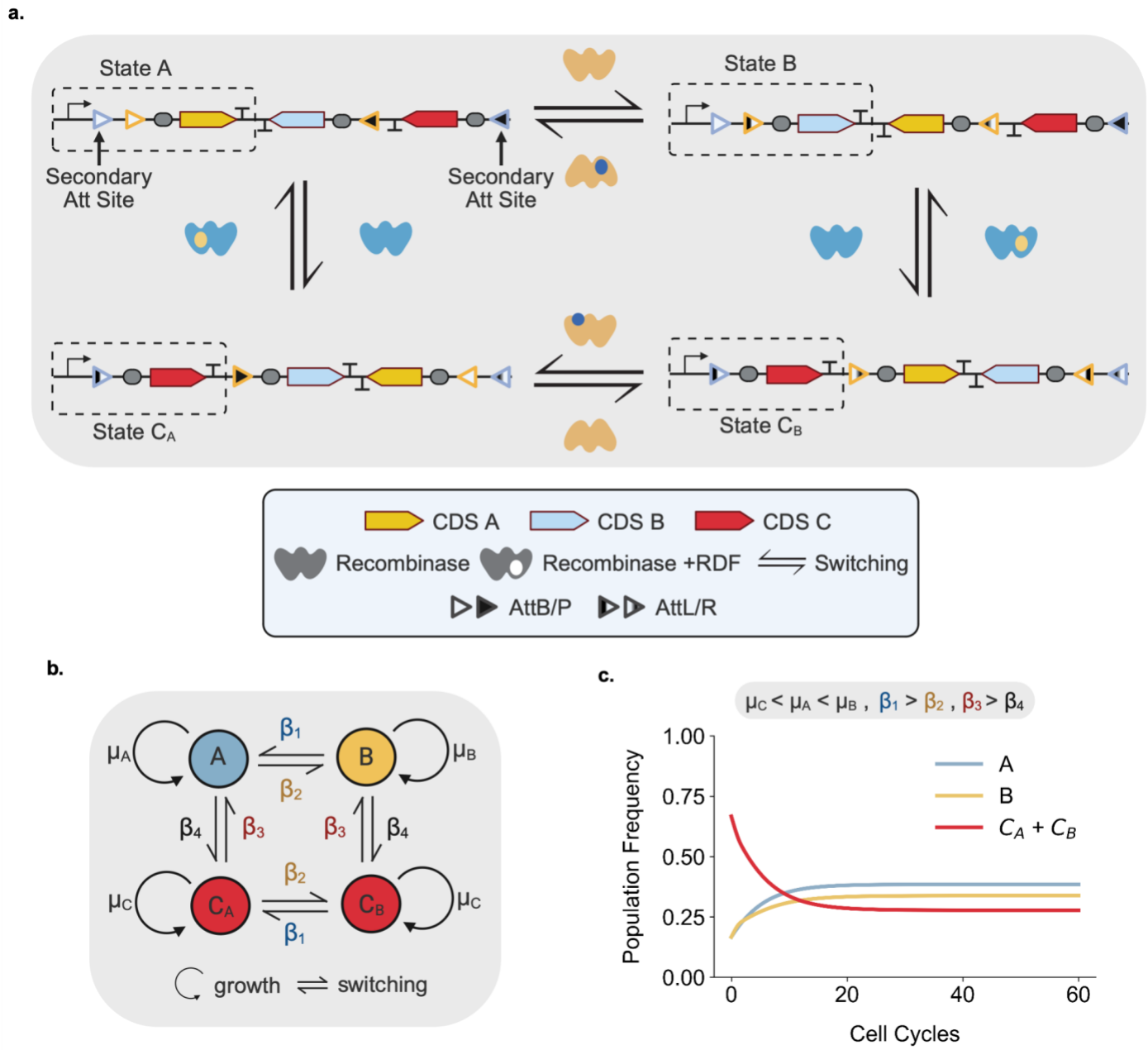

Figure 5. A second recombinase allows 3-state switching. a, Recombinase elements (include Att sites) are colored according to their cognate recombinase. Arrows represent transitions between states, with the relevant recombinase complex catalyzing these transitions next to each arrow. The active transcriptional state of the system is surrounded by a dotted box. Note C_A and C_B are two separate DNA states but transcriptionally are the same state. **b** 3-state phase varying consortium schematic. Note that certain transition rates catalyze multiple distinct transitions e.g. β_1 switches B to A and C_B to C_A. **c** 3-state model simulation dynamics. Presented results and parameters are non-dimensionalized and scaled to the growth rate of strain/phenotype C. Further details on modeling and simulations can be found in the modeling supplement.

296 **A recombinase circuit experimentally demonstrates 3-state phase variation**
297 To implement the 3-state circuits, we added a second orthogonal recombinase and RDF, TP901[49]
298 together with a third fluorescent protein, mScarlet3[50]. TP901 and its cognate RDF were placed
299 under the control of the lux and cin inducible promoters[45], respectively and assembled alongside
300 the Bxb1 elements (Fig. 6a). We examined the system in the mother machine, using similar
301 growth conditions to the 2-state system (Fig. 6b, Methods). Cells switched across all three
302 fluorophore states, presenting stable expression of each fluorescent state. However, in contrast
303 to the 2-state system, the 3-state circuit imposed a larger burden on cell physiology, leading to
304 filementation and cell death (Supplemental Movie 2). This was partially remedied by reducing the
305 copy number of the recombinase elements by moving the circuit from a p15a plasmid to a genomic
306 location (pOSIP T-site)[51]. This alteration successfully reduced burden. It also markedly increased
307 the single cell switching timescale, consistent with lower recombinase expression levels
308 (Supplemental Movie 3-7). Nonetheless, the 3-state system exhibited active switching among
309 three stable, heritable expression states.
310
311 Finally, we characterized composition control at the bulk level. We initiated cultures from an all-
312 YFP initial composition. We identified several inducer conditions that enabled stable, long-term
313 coexistence (~120 hours) of all states (Fig. 6d, Supplementary Fig. 23-24). This contrasts with a
314 non-switching control system, where the mScarlet strain rapidly takes over the mixed culture
315 (Supplementary Fig. 25). Interestingly, the two switching processes in our system operate at
316 different timescales, with the YFP to mTurquoise (Bxb1) process reaching equilibrium noticeably
317 faster than the (YFP + mTurquoise) to mScarlet process. These experiments demonstrated that
318 synthetic phase variation circuits can create a stable set of compositions in an otherwise unstable
319 3-state system.
320
321 Finally, having investigated stable compositions, we asked what transient composition trajectories
322 were accessible. We used a similar passaging setup, but assayed a wider variety of inducer
323 concentrations over fewer passages (Supplementary Table 1). Under these conditions, increasing
324 salicylate concentration (Bxb1) increased mTurquoise signal and increasing lux AHL (TP901)
325 increased mScarlet signal, indicating that the system continued to function as expected. The 3-
326 state system traversed a broad variety of compositions (Fig. 6e, Supplementary Fig. 13-22).
327 Cultures transiently populated compositions heavily biased towards individual states (closer to
328 vertices), as well as mixed compositions (closer to grey center triangle). Depending on the
329 conditions, cells traversed the composition space at different velocities. These experiments
330 demonstrate that we can transiently pass through a wide variety of compositions.

331

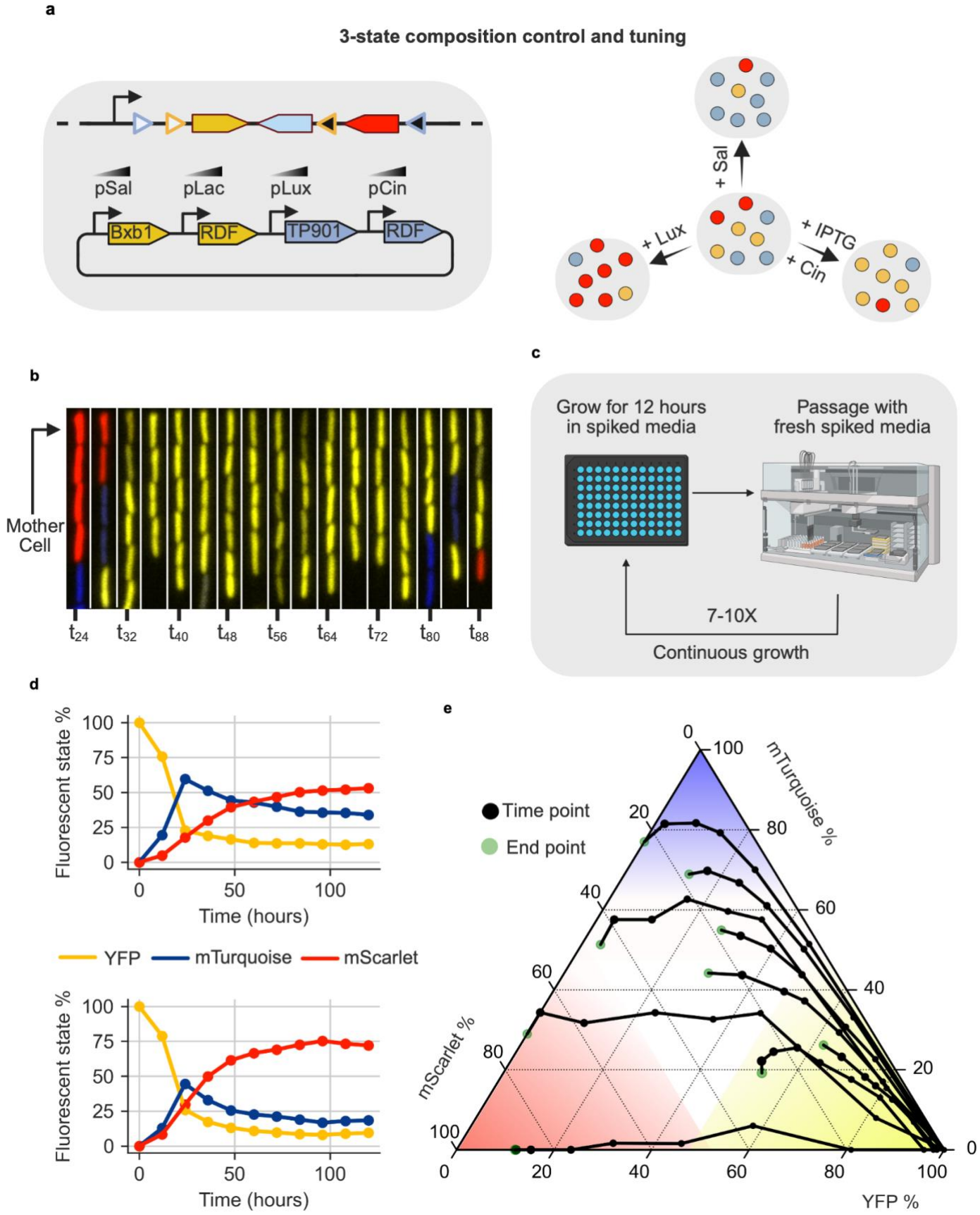
a
3-state composition control and tuning
pSal
pLac
pLux
pCin
Bxb1
RDF
TP901
RDF
+ Sal
+ Lux
+ IPTG
+ Cin
b
Mother Cell
t24
t32
t40
t48
t56
t64
t72
t80
t88
c
Grow for 12 hours in spiked media
Passage with fresh spiked media
7-10X
Continuous growth
d
Fluorescent state %
Time (hours)
YFP
mTurquoise
mScarlet
e
Time point
End point
mTurquoise %
mScarlet %
YFP %

Figure 6. The 3-state design retains the single cell and bulk dynamics of the 2-state system. **a** 3-state composition control schematic. Recombinase elements (include Att sites) are colored according to their cognate recombinase. The 3-state switching construct is integrated as a single copy on the genome. Bxb1 is controlled by a salicylate inducible promoter (pSal) and its cognate RDF is controlled by an IPTG inducible promoter pTac. TP901 is controlled by a Lux AHL (pLux) inducible promoter and its cognate RDF is controlled by a Cin AHL inducible promoter (pCin). By varying inducer levels, the steady state composition of the system should be tunable. The copy number of the recombinase element varies based on the experiment. **b** Mother machine kymograph. Successive images are separated by forty minute intervals. **c** Liquid handler passaging setup. **d** Select stable 3-state time course traces. Fluorescence values have been normalized to the max possible fluorescence signal for the given channel. **e** 3-state space exploration traces. Fluorescence values have been normalized to the max possible fluorescence signal for the given channel. As typical for a ternary diagram, the ratio of all three channels is used to calculate positions of individual trajectories. Each point in a given trajectory is separated by a fixed growth cycle of 12 hours.

Discussion

The ability to establish defined distributions of cell states within a population would facilitate the creation of stable microbial communities. It has, however, remained unclear if a recombinase approach could tune phenotypic variation for multiple distinct states, and improve upon the tunability and scalability of toggle switches[48,52,53] and other previous approaches[14,22,23]. Here, we demonstrated granular, straightforward control of two to three distinct phenotypic states. Further, this strategy could be scaled to higher numbers of states by adding additional recombinases. Thus, it should be possible to engineer multi-state consortia within a single strain.

There are several limitations of this work. First, recombinases place a burden on cell physiology[54–56]. Better understanding this burden and developing ways to circumvent it will be important for its deployment in applications. Specifically, characterizing the interplay between recombinase expression, switching rates, bulk dynamics and burden will be critical. Optimizing burden is a particular concern as a given composition control method should be as low-burden as possible to minimize interference with consortia function. However, the circuits introduced here displayed high levels of burden in the mother machine, with noticeable cell death and filamentation, especially in the 3-state system (Supplemental Movie 2). These effects were reduced but not eliminated by reducing the copy number of the recombinase genes. In this architecture, the number of unique controllable states scales linearly with the number of distinct recombinases. There are over 60 characterized serine recombinases[35], many of which are orthogonal but the larger issue relates to the burden associated with each additional recombinase. This could be partially addressed through mutant recombinase attachment sites that switch at faster rates than their wild-type counterparts[57], reducing the required recombinase expression level, while maintaining higher switching rates. Another fundamental limitation of our approach is shared with the terminal differentiation approach: the cell must be capable of expressing each phenotype in the system. This prevents use of multi-species consortia and runs counter to the typical strain specialization workflows of metabolic engineering[8,11].

Synthetic phase variation could be expanded in several ways. First, one could decouple the core state switching circuit from the target genes it controls. Specifically, fluorescent protein genes could be replaced with transcriptional activators that would in turn regulate expression of functional transcriptional units on separate genetic constructs. Those transcriptional units would not need to be expressed as single copies. This modification would improve modularity, allowing for easy swapping of functional target genes. Second, a unique element of our circuit is that it could be implemented in mammalian systems, where recombinase activity has previously been demonstrated[58]. Further, unlike communication-mediated composition control, the circuit introduced here does not rely on synthesis or active import and export of metabolites, making it theoretically more host-agnostic than other approaches. It will be interesting to find out whether the circuit can be modified to operate in human cells for research and applications. The approach introduced here could potentially be implemented in non-model microorganisms for rapid development of non-model organism consortia, e.g. *Pseudomonas* species for soil[59] and *Bacteroides* for gut[60].

Synthetic phase variation circuits enable several specific applications. Because cells retain access to all states and control can be maintained without intercellular communication, composition control should be spatially invariant and deployable in non-well-mixed, even static, environments. For instance, bioprocessing has benefited from use of consortia[46,61–63]. However, at the industrial scale many fermentations have issues with spatial heterogeneity and mixing[19]. This interferes with the use of communication-mediated consortia; our approach would be able to maintain control in this context. Similarly, gut microbiome engineering could be heavily enabled through the use of consortia, with different phenotypes interacting with specific niches to cause persistent, large scale shifts in the microbiome[64]. However, the gut displays erratic and irregular mixing, favouring the use of our approach to implement consortia in the gut microbiome[20]. Another suitable use of our system may be in the context of biomaterials. Specifically, several biomaterials systems use varying ratios of different strains/phenotypes to generate materials with differing mechanical properties[65,66]. In our framework, a single cell would be able to generate all phenotypes, implying one could regenerate a biomaterial from a single cell sample. This regeneration phenomena would be infeasible to recreate using the communication-mediated or terminal differentiation approaches.

Stochasticity is often perceived as a nuisance that degrades the performance of synthetic biological circuits. In this case, stochasticity is essential to generate stable, accurate composition at the population level. This design provides an example of how naturally inspired circuits can be used to exploit unique biological phenomena to generate novel engineered functions.

416 **Strain and plasmid construction**
417 A list of all fragments, constructs and strains used in this study can be found in Supplementary
418 File 1. The associated sequences have been uploaded as part of the supplemental files. The
419 MG1655 Marionette strain was used as the base strain for all experiments in this study. Genomic
420 integrations for this study were performed using the pOSIP clonetegration system. For mother
421 machine experiments, knockouts of the MotA gene were necessary and were performed using
422 Lambda Red Recombineering.
423
424 All plasmids were assembled using 3G assembly[1], sourcing parts from Murray Biocircuits Part
425 Library, an extended version of the CIDAR MoClo extension part kit. To perform pOSIP
426 clonetegration of switching constructs, an approach alternating use of bsaI (NEBuilder® HiFi DNA
427 Assembly Master Mix) and bsmbI (NEBridge® Golden Gate Assembly Kit (BsmBI-v2)) to catalyze
428 golden gate assembly constructs was employed. Other pOSIP clonetegrations were performed
429 using 3G assembly.
430
431 **Media and Reagents**
432 For plate reader experiments, cells were grown in M9CA 1% glucose (Teknova) with 25 µg/ml
433 chloramphenicol and 50 µg/ml kanamycin. For mother machine experiments cells were grown in
434 M9CA 0.5% glycerol with 25 µg/ml chloramphenicol, 50 µg/ml kanamycin and 50 µg/ml
435 hygromycin. Unlike the glucose media, the glycerol media was not purchased from a vendor and
436 made in the wetlab. 1L of this media was produced using 200 ml of 5X M9 Salts, 10 ml 50%
437 glycerol solution (Teknova), 10 ml 100X casamino acid solution, 1 ml 1000X thiamine-HCL
438 solution, 200 µl 5000X $MgSO_4$ solution and 100 µl 10000X $CaCl_2$ solution. The quantities of each
439 chemical and solvent required to make these stock solutions can be found in the table below.
440

Solution name	Chemical name and quantity	Solvent name and quantity
5X M9 Salts	56.4 g M9 Salts	1L distilled water
100X Casamino acid	20 g Casamino acids	200 mL distilled water
1000X Thiamine	10 mg Thiamine-HCl	20 mL distilled water
5000X $MgSO_4$	2.465 mg $MgSO_4$-$7H_2O$	10 mL distilled water
10000X $CaCl_2$	1.10 mg $CaCl_2$-$2H_2O$	10 mL distilled water

441
442

443 **Mother machine experiment preparation**
444 Microfluidic 'mother machine' devices were manufactured in the Jun Lab at UCSD according to
445 the protocol from Wang et al.[2] Prior to loading cells, the device was annealed to a WillCo-dish
446 (Glass Bottom Dish, HBST-5040) via high power plasma cleaning. Once annealed, the device
447 was loaded with 10 µl of 0.5 mg mL^{-1} BSA (Bovine serum albumin).
448
449 From an overnight culture of the relevant strain grown in M9CA Glycerol (w/ antibiotics) , 20 µl of
450 culture was diluted into 1 ml of fresh M9CA Glycerol (w/ antibiotics) and grown at 37 °C for 4
451 hours. After 4 hours, the culture was centrifuged and resuspended to concentrate cells 10-fold.
452 10 µl of this concentrated culture was then loaded into the BSA-treated mother machine device
453 main trench. To load cells into the channels of the mother machine, the device was then placed
454 (via custom adapters) into a centrifuge and spun for two minutes on each side of the device,
455 loading cells into channels on both sides of the main trench. Once cells were loaded, small
456 volumes of inducer spiked media were loaded from the syringe into the mother machine device
457 to clear the main trench of cell debris and provide media for cells.
458
459 **Mother machine analysis**
460 To correct temperature related drift during the mother machine experiments, the 'Correct 3D Drift'
461 plugin in FIJI[3] was employed for each FOV. Stabilized FOVs were then cropped and resized to
462 ensure identical pixel dimensions across FOVs. FOVs were then analyzed and segmented in the
463 napari-mm3 software[4] developed by the Jun Lab.
464
465 The subsequent described steps were performed in python and the scripts applying these steps
466 to the segmented dataset can be found at the following GitHub repository. With the segmented
467 outputs of the napari-mm3 pipeline, the cells masks were applied to the YFP and mTurquoise
468 fluorescent channels. After background subtraction and normalization to the maximum signal of
469 each fluorophore, intensities for each cell were summed. If this sum was below 0.25, the cell was
470 assumed to be non-fluorescent and not included in further analysis. Cells that passed this
471 screening step had the ratio of normalized mTurquoise intensity to normalized YFP intensity
472 calculated. Using thresholds based on observations of movies, a cell was considered mTurquoise
473 if this ratio was above 2, YFP if this ratio was below 0.5 and mixed if between these two values.
474 To calculate the steady-state composition, we used the average $\log_{10}$(YFP/mTurquoise) signal
475 for the last 3 hours of each experimental sample. To calculate the time to 95% steady-state, we
476 located the first time point where $\log_{10}$(YFP/mTurquoise) was within 5% of the aforementioned
477 steady state.
478
479 For the mother cell trace in Fig 3., on the stabilized movie of the relevant trench, a region of
480 interest in FIJI was drawn that encapsulated exclusively the mother cell. The 'Measure Stack'
481 function was then used to collect intensities in this ROI. The max values of each channel across
482 time were then smoothed using the Savitzky-Golay filter implementation in SciPy[5].
483
484

485 **Composition control plate reader experiments (2-state)**
486 Unless otherwise specified, all cultures were grown in 96 square well plates (96 well MatriPlate ™
487 clear bottom), in M9CA Glucose with kanamycin and chloramphenicol, at 37 °C using a plate
488 reader (Biotek H1M). From an overnight culture of the 2-state system, three separate wells with
489 different spiked media were seeded and grown overnight. These three wells were then spun down
490 to remove inducers and resuspended in fresh media. 65 ul of these resuspended cultures were
491 then added to 299 ul of fresh unspiked media and grown in a plate reader until they reached an
492 OD_{700} of 0.65. At this OD, the liquid handler (Hamilton STARlet Liquid Handling Robot) removed
493 the culture plate and seeded a new culture for each of the three wells. These new cultures were
494 composed of 299 µl spiked media and 64 µl of the previous culture. The culture plate was then
495 replaced into the plate reader, repeating this culture seeding process once the newest culture
496 reached an OD_{700} of 0.65.
497
498 Due to the time-varying, pulsatile production of the deg-tagged fluorophores in batch culture, the
499 max YFP and mTurquoise fluorescent signal pulse in a given growth well was taken as the
500 abundance of a given state. After background subtraction, these values were used to calculate
501 the ratio of YFP to mTurquoise signal. To calculate the steady-state composition, we used the
502 average $\log_{10}$(YFP/mTurquoise) signal for the last timepoint across the three replicates for a given
503 induction condition. To calculate the time to 95% steady-state, we located the first time point
504 where $\log_{10}$(YFP/mTurquoise) was within 5% of the aforementioned steady state.
505
506 **Composition control plate reader experiments (3-state)**
507 From an overnight culture of the 3-state system, a single well with spiked media was seeded and
508 grown in the plate reader at 37°C. After 12 hours, the plate was removed and 2 µl of cells from
509 the grown well was transferred to a new well with 200 µl fresh spiked media, maintaining the same
510 concentrations of spiked inducers in these new wells. This lower dilution ratio was selected as it
511 seemed to cause a marked improvement in cell health and circuit function. For stable, long time
512 courses (Fig 6d), this dilution occurred 9 times for a total observed growth time of approximately
513 10X12 hrs. For space exploration time courses (Fig 6e), this dilution occurred 7 times for a total
514 observed growth time of approximately 7X12 hrs.
515
516 Due to the time-varying production of the deg-tagged fluorophores in batch culture, the max YFP,
517 mScarlet and mTurquoise fluorescent signal in a given growth well was taken as the abundance
518 of a given state. Due to drastically differing max intensities of each state, after background
519 subtraction, the max signal was normalized to the maximum possible intensity of the relevant
520 fluorescent state. These max intensities were determined by completely biasing the system to the
521 relevant fluorescent state. These subtracted and normalized values were then used to plot the
522 ternary diagram in Figure 6.
523
524 **Data and code for computational analysis**
525 Qualitative descriptions of computational analysis performed are present in each subsection of
526 the methods. Data used for analysis and scripts executing said analysis can be found in the Github
527 repository associated with this manuscript.
528

529 **References**

530 1. McCarty, N. S. & Ledesma-Amaro, R. Synthetic Biology Tools to Engineer Microbial
531 Communities for Biotechnology. *Trends Biotechnol.* **37**, 181–197 (2019).
532 2. Brenner, K., You, L. & Arnold, F. H. Engineering microbial consortia: a new frontier in
533 synthetic biology. *Trends Biotechnol.* **26**, 483–489 (2008).
534 3. Duncker, K. E., Holmes, Z. A. & You, L. Engineered microbial consortia: strategies and
535 applications. *Microb. Cell Factories* **20**, 211 (2021).
536 4. Roell, G. W. *et al.* Engineering microbial consortia by division of labor. *Microb. Cell*
537 *Factories* **18**, 35 (2019).
538 5. Mittermeier, F. *et al.* Artificial microbial consortia for bioproduction processes. *Eng. Life*
539 *Sci.* **23**, e2100152 (2023).
540 6. Jawed, K., Yazdani, S. S. & Koffas, M. AG. Advances in the development and
541 application of microbial consortia for metabolic engineering. *Metab. Eng. Commun.* **9**,
542 e00095 (2019).
543 7. Bhatia, S. K. *et al.* Biotechnological potential of microbial consortia and future
544 perspectives. *Crit. Rev. Biotechnol.* **38**, 1209–1229 (2018).
545 8. Xin, Y. & Qiao, M. Towards microbial consortia in fermented foods for metabolic
546 engineering and synthetic biology. *Food Res. Int.* **201**, 115677 (2025).
547 9. Jiang, Y., Wu, R., Zhang, W., Xin, F. & Jiang, M. Construction of stable microbial
548 consortia for effective biochemical synthesis. *Trends Biotechnol.* **41**, 1430–1441 (2023).
549 10. Sagt, C. M. J. Systems metabolic engineering in an industrial setting. *Appl. Microbiol.*
550 *Biotechnol.* **97**, 2319–2326 (2013).
551 11. Sun, J. & Alper, H. S. Metabolic engineering of strains: from industrial-scale to lab-scale
552 chemical production. *J. Ind. Microbiol. Biotechnol.* **42**, 423–436 (2015).
553 12. Balagaddé, F. K. *et al.* A synthetic Escherichia coli predator-prey ecosystem. *Mol. Syst.*
554 *Biol.* **4**, 187 (2008).

555 13. McCardell, R. D., Pandey, A. & Murray, R. M. Control of density and composition in an
556 engineered two-member bacterial community. 632174 Preprint at
557 https://doi.org/10.1101/632174 (2019).
558 14. You, L., Cox, R. S., Weiss, R. & Arnold, F. H. Programmed population control by cell–
559 cell communication and regulated killing. *Nature* **428**, 868–871 (2004).
560 15. Kong, W., Meldgin, D. R., Collins, J. J. & Lu, T. Designing microbial consortia with
561 defined social interactions. *Nat. Chem. Biol.* **14**, 821–829 (2018).
562 16. Scott, S. R. *et al.* A stabilized microbial ecosystem of self-limiting bacteria using
563 synthetic quorum-regulated lysis. *Nat. Microbiol.* **2**, 1–9 (2017).
564 17. Xu, P. Dynamics of microbial competition, commensalism, and cooperation and its
565 implications for coculture and microbiome engineering. *Biotechnol. Bioeng.* **118**, 199–209
566 (2021).
567 18. Wintermute, E. H. & Silver, P. A. Emergent cooperation in microbial metabolism. *Mol.*
568 *Syst. Biol.* **6**, 407 (2010).
569 19. Lara, A. R., Galindo, E., Ramírez, O. T. & Palomares, L. A. Living with heterogeneities in
570 bioreactors: understanding the effects of environmental gradients on cells. *Mol. Biotechnol.*
571 **34**, 355–381 (2006).
572 20. Labavić, D., Loverdo, C. & Bitbol, A.-F. Hydrodynamic flow and concentration gradients
573 in the gut enhance neutral bacterial diversity. *Proc. Natl. Acad. Sci.* **119**, e2108671119
574 (2022).
575 21. Williams, R. L. & Murray, R. M. Integrase-mediated differentiation circuits improve
576 evolutionary stability of burdensome and toxic functions in E. coli. *Nat. Commun.* **13**, 6822
577 (2022).
578 22. Aditya, C., Bertaux, F., Batt, G. & Ruess, J. A light tunable differentiation system for the
579 creation and control of consortia in yeast. *Nat. Commun.* **12**, 5829 (2021).
580 23. An, B. *et al.* Synthetic ratio computation for programming population composition and

581 multicellular morphology. 2024.11.26.624747 Preprint at
582 https://doi.org/10.1101/2024.11.26.624747 (2024).
583 24. Thattai, M. & van Oudenaarden, A. Stochastic Gene Expression in Fluctuating
584 Environments. *Genetics* **167**, 523–530 (2004).
585 25. van der Woude, M. W. & Bäumler, A. J. Phase and Antigenic Variation in Bacteria. *Clin.*
586 *Microbiol. Rev.* **17**, 581–611 (2004).
587 26. Morawska, L. P., Hernandez-Valdes, J. A. & Kuipers, O. P. Diversity of bet-hedging
588 strategies in microbial communities—Recent cases and insights. *Wires Mech. Dis.* **14**,
589 e1544 (2022).
590 27. Wolf, D. M., Vazirani, V. V. & Arkin, A. P. Diversity in times of adversity: probabilistic
591 strategies in microbial survival games. *J. Theor. Biol.* **234**, 227–253 (2005).
592 28. Visco, P., Allen, R. J., Majumdar, S. N. & Evans, M. R. Switching and Growth for
593 Microbial Populations in Catastrophic Responsive Environments. *Biophys. J.* **98**, 1099–1108
594 (2010).
595 29. Jia, C., Qian, M.-P., Kang, Y. & Jiang, D.-Q. Modeling stochastic phenotype switching
596 and bet-hedging in bacteria: stochastic nonlinear dynamics and critical state identification.
597 Preprint at https://doi.org/10.48550/arXiv.1311.2216 (2015).
598 30. Pédelacq, J.-D., Cabantous, S., Tran, T., Terwilliger, T. C. & Waldo, G. S. Engineering
599 and characterization of a superfolder green fluorescent protein. *Nat. Biotechnol.* **24**, 79–88
600 (2006).
601 31. Goedhart, J. *et al.* Structure-guided evolution of cyan fluorescent proteins towards a
602 quantum yield of 93%. *Nat. Commun.* **3**, 751 (2012).
603 32. Jadhav, P., Chen, Y., Butzin, N., Buceta, J. & Urchueguía, A. Bacterial degrons in
604 synthetic circuits. *Open Biol.* **12**, 220180 (2022).
605 33. Stark, W. M. Making serine integrases work for us. *Curr. Opin. Microbiol.* **38**, 130–136
606 (2017).

607 34. Olorunniji, F. J. *et al.* Gated rotation mechanism of site-specific recombination by ϕC31
608 integrase. *Proc. Natl. Acad. Sci.* **109**, 19661–19666 (2012).
609 35. Durrant, M. G. *et al.* Systematic discovery of recombinases for efficient integration of
610 large DNA sequences into the human genome. *Nat. Biotechnol.* **41**, 488–499 (2023).
611 36. Yang, L. *et al.* Permanent genetic memory with >1-byte capacity. *Nat. Methods* **11**,
612 1261–1266 (2014).
613 37. Bonnet, J., Subsoontorn, P. & Endy, D. Rewritable digital data storage in live cells via
614 engineered control of recombination directionality. *Proc. Natl. Acad. Sci.* **109**, 8884–8889
615 (2012).
616 38. Huang, B. D., Kim, D., Yu, Y. & Wilson, C. J. Engineering intelligent chassis cells via
617 recombinase-based MEMORY circuits. *Nat. Commun.* **15**, 2418 (2024).
618 39. Hung, M. *et al.* Modulating the frequency and bias of stochastic switching to control
619 phenotypic variation. *Nat. Commun.* **5**, 4574 (2014).
620 40. Wang, P. *et al.* Robust growth of Escherichia coli. *Curr. Biol. CB* **20**, 1099–1103 (2010).
621 41. Bakshi, S. *et al.* Tracking bacterial lineages in complex and dynamic environments with
622 applications for growth control and persistence. *Nat. Microbiol.* **6**, 783–791 (2021).
623 42. Luro, S., Potvin-Trottier, L., Okumus, B. & Paulsson, J. Isolating live cells after high-
624 throughput, long-term, time-lapse microscopy. *Nat. Methods* **17**, 93–100 (2020).
625 43. Sauls, J. T. *et al.* Control of Bacillus subtilis Replication Initiation during Physiological
626 Transitions and Perturbations. *mBio* **10**, 10.1128/mbio.02205-19 (2019).
627 44. Si, F. *et al.* Mechanistic Origin of Cell-Size Control and Homeostasis in Bacteria. *Curr.
628 Biol.* **29**, 1760-1770.e7 (2019).
629 45. Meyer, A. J., Segall-Shapiro, T. H., Glassey, E., Zhang, J. & Voigt, C. A. Escherichia coli
630 “Marionette” strains with 12 highly optimized small-molecule sensors. *Nat. Chem. Biol.* **15**,
631 196–204 (2019).
632 46. Jones, J. A. *et al.* Complete Biosynthesis of Anthocyanins Using E. coli Polycultures.

633 *mBio* **8**, e00621-17.
634 47. Zhu, R., del Rio-Salgado, J. M., Garcia-Ojalvo, J. & Elowitz, M. B. Synthetic multistability
635 in mammalian cells. *Science* **375**, eabg9765 (2022).
636 48. Wu, F., Su, R.-Q., Lai, Y.-C. & Wang, X. Engineering of a synthetic quadrastable gene
637 network to approach Waddington landscape and cell fate determination. *eLife* **6**, e23702
638 (2017).
639 49. Christiansen, B., Brøndsted, L., Vogensen, F. K. & Hammer, K. A resolvase-like protein
640 is required for the site-specific integration of the temperate lactococcal bacteriophage
641 TP901-1. *J. Bacteriol.* **178**, 5164–5173 (1996).
642 50. Gadella, T. W. J. *et al.* mScarlet3: a brilliant and fast-maturing red fluorescent protein.
643 *Nat. Methods* **20**, 541–545 (2023).
644 51. St-Pierre, F. *et al.* One-Step Cloning and Chromosomal Integration of DNA. *ACS Synth.*
645 *Biol.* **2**, 537–541 (2013).
646 52. Guarino, A., Fiore, D., Salzano, D. & di Bernardo, M. Balancing Cell Populations
647 Endowed with a Synthetic Toggle Switch via Adaptive Pulsatile Feedback Control. *ACS*
648 *Synth. Biol.* **9**, 793–803 (2020).
649 53. Salzano, D., Fiore, D. & di Bernardo, M. *Controlling Reversible Cell Differentiation for*
650 *Labor Division in Microbial Consortia*.
651 http://biorxiv.org/lookup/doi/10.1101/2021.08.03.454926 (2021)
652 doi:10.1101/2021.08.03.454926.
653 54. Grob, A., Di Blasi, R. & Ceroni, F. Experimental tools to reduce the burden of bacterial
654 synthetic biology. *Curr. Opin. Syst. Biol.* **28**, 100393 (2021).
655 55. Sechkar, K., Steel, H., Perrino, G. & Stan, G.-B. A coarse-grained bacterial cell model
656 for resource-aware analysis and design of synthetic gene circuits. *Nat. Commun.* **15**, 1981
657 (2024).
658 56. Liu, Q., Schumacher, J., Wan, X., Lou, C. & Wang, B. Orthogonality and Burdens of

659 Heterologous AND Gate Gene Circuits in E. coli. *ACS Synth. Biol.* **7**, 553–564 (2018).
660 57. Zhang, Q., Azarin, S. M. & Sarkar, C. A. Model-guided engineering of DNA sequences
661 with predictable site-specific recombination rates. *Nat. Commun.* **13**, 4152 (2022).
662 58. Farruggio, A. P., Chavez, C. L., Mikell, C. L. & Calos, M. P. Efficient reversal of phiC31
663 integrase recombination in mammalian cells. *Biotechnol. J.* **7**, 1332–1336 (2012).
664 59. Larsson, E. M., Murray, R. M. & Newman, D. K. Engineering the Soil Bacterium
665 Pseudomonas synxantha 2–79 into a Ratiometric Bioreporter for Phosphorus Limitation.
666 *ACS Synth. Biol.* **13**, 384–393 (2024).
667 60. Mimee, M., Tucker, A. C., Voigt, C. A. & Lu, T. K. Programming a Human Commensal
668 Bacterium, Bacteroides thetaiotaomicron, to Sense and Respond to Stimuli in the Murine
669 Gut Microbiota. *Cell Syst.* **1**, 62–71 (2015).
670 61. Wang, F. *et al.* One-pot biocatalytic route from cycloalkanes to α,ω-dicarboxylic acids by
671 designed Escherichia coli consortia. *Nat. Commun.* **11**, 5035 (2020).
672 62. Wang, X. *et al.* Engineering a Microbial Consortium Based Whole-Cell System for
673 Efficient Production of Glutarate From L-Lysine. *Front. Microbiol.* **10**, 341 (2019).
674 63. Zhang, Z. *et al.* One-pot biosynthesis of 1,6-hexanediol from cyclohexane by de novo
675 designed cascade biocatalysis. *Green Chem.* **22**, 7476–7483 (2020).
676 64. Nazir, A., Hussain, F. H. N. & Raza, A. Advancing microbiota therapeutics: the role of
677 synthetic biology in engineering microbial communities for precision medicine. *Front.*
678 *Bioeng. Biotechnol.* **12**, 1511149 (2024).
679 65. An, B. *et al.* Programming Living Glue Systems to Perform Autonomous Mechanical
680 Repairs. *Matter* **3**, 2080–2092 (2020).
681 66. Gilbert, C. & Ellis, T. Biological Engineered Living Materials: Growing Functional
682 Materials with Genetically Programmable Properties. *ACS Synth. Biol.* **8**, 1–15 (2019).
683
684

Acknowledgments

We thank John Marken, Manisha Kapasiawala, Ethan Richman and Evan Mun as well as other members of the Murray and Elowitz Lab for their feedback on this manuscript. We also thank the various members of the Jun Lab, especially Michael Sandler and Haochen Fu for hosting Matthieu in their lab for the mother machine experiments. This material is based upon work funded by the Caltech Rosen Bioengineering Center and the Caltech Center for Environmental Microbial Interaction. MBE is an investigator of the Howard Hughes Medical Institute.

Contributions

MFK conceived and designed the project, performed the experiments, analyzed the data, and wrote the paper, all under the supervision of MBE and RMM.

Competing Interests

The authors declare no competing interests for the work in this paper.